International Journal of Nanomedicine Dovepress

Open Access Full Text Article ORIGINAL RESEARCH

pH-Responsive Charge-Reversal Smart Nanoparticles for Co-Delivery of Mitoxantrone and Copper Ions to Enhance Breast Cancer Chemo-Chemodynamic Combination Therapy

Tao Tan[1,*], Weiyi Chang[1,2,*], Tian Long Wang[1], Wei Chen[1], Xiaobing Chen[1], Chunmiao Yang[1], Dongsheng Yang[1]

[1]College of Life Science, Zhuhai College of Science and Technology, Zhuhai, 519041, People's Republic of China; [2]College of Life Science, Jilin University, Changchun, 130012, People's Republic of China

*These authors contributed equally to this work

Correspondence: Dongsheng Yang, College of Life Science, Zhuhai College of Science and Technology, Zhuhai, 519041, People's Republic of China, Email yds@zcst.edu.cn

Purpose: The poor delivery and limited penetration of nanoparticles into breast cancer tumors remain essential challenges for effective anticancer therapy. This study aimed to design a promising nanoplatform with efficient tumor targeting and penetration capability for effective breast cancer therapy.

Methods: A pH-sensitive mitoxantrone (MTO) and copper ion-loaded nanosystem functionalized with cyclic CRGDfK and r9 peptide (TPRN-CM) was rationally designed for chemo-chemodynamic combination therapy. TPRN-CM would be quiescent in blood circulation with the CRGDfK peptide on the surface of the nanoparticle to improve its targeting to the tumor. Then, the structure of TPRN-CM changes in the acidic tumor microenvironment, and the r9 peptide can be exposed to make a surface charge reversal to promote deep penetration in the tumor and facilitate their internalization by cancer cells, which was characterized using transmission electron microscopy, dynamic light scattering, flame atomic absorption, etc. The drug release behavior, anti-tumor effects in vivo and in vitro, and the biosafety of the nanoplatform were evaluated.

Results: TPRN-CM exhibited remarkable capability to load MTO and Cu^{2+} with good stability in serum. It can achieve pH-responsive charge reversal, MTO, and Cu^{2+} release, and can further generate toxic hydroxyl radicals in the presence of glutathione (GSH) and H_2O_2. In vitro experiments demonstrated that this nanoplatform significantly inhibited proliferation, migration, invasion activities and 3D-tumorsphere growth. In vivo experiments suggested that rationally designed TPRN-CM can be effectively delivered to breast cancer tumors with deep tumor penetration, thereby resulting in a notable reduction in tumor growth and suppression of lung metastasis without causing any apparent side effects.

Conclusion: The constructed TPRN-CM nanoplatform integrated tumor targeting, tumor penetration, drug-responsive release, and chemo-chemodynamic combination therapy, thereby providing an intelligent drug delivery strategy to improve the efficacy of breast cancer treatment.

Keywords: pH-responsive, charge-reversal, chemo-chemodynamic combination therapy, penetration, breast cancer

Introduction

Chemotherapy is widely used to treat breast cancer in clinical practice, but the chemoresistance and adverse effects of poor selectivity on cancer tissue severely limit their clinical application.[1] Developed nanomedicines can realize tumor specific delivery through active or passive targeting, but their therapeutic effects are not satisfactory.[2] At present, multiple treatments with synergistic anti-tumor effects have good development prospects.[3–6] Chemodynamic therapy (CDT) based on Fenton chemistry has gradually become a new type of cancer treatment, utilizing the Fenton-like reaction to convert

Received: 1 August 2024
Accepted: 24 October 2024
Published: 7 November 2024

hydrogen peroxide (H_2O_2) in tumors into highly toxic hydroxyl radicals (•OH, one of the reactive oxygen species (ROS)) for specifically killing tumor cells.[7] Compared with other ROS therapies, the CDT has advantages such as higher catalytic performance in generating ROS, less dependence on external stimuli, and deep tissue therapeutic ability. Interestingly, the generated ROS can improve the therapeutic effects of chemotherapeutic drugs,[8,9] suggesting that the synergistic combination of CDT and chemotherapy could treat tumor progression and metastasis.[10–13]

Nanosystems can serve as powerful delivery platforms for simultaneously loading chemotherapy and CDT agents,[3,14,15] and can effectively target tumors by taking advantage of the enhanced permeability and retention effects.[16] However, most of these nanosystems are mainly detected in the external regions of tumor tissues rather than penetrating the deep inner sides, resulting in inadequate therapeutic efficacy.[17–19] Typically, the delivery efficiency of nanosystems depends on the biological barrier and how they interact with barriers before reaching the target site. The solid tumor of breast cancer posses the main barrier called the tumor microenvironment (TME), mainly including extracellular matrix (ECM), the disorganized tumor vascular network, stromal cells (SCs, tumor-associated macrophage (TAM), cancer-associated fibroblasts (CAFs)), and so on.[20] The biological barrier formed by the abundant CAFs and excessive ECM on the periphery of tumor tissues results in poor distribution and penetration of drugs and nanoparticles.[21] For chemotherapy and CDT, the poor tumor penetration of the nanodrugs can lead to heterogeneous distribution of drug in tumor, thereby resulting in failure to completely eradicate the tumor.[22,23] Many materials including cationic polymer and lipid, or peptides, etc are under exploration for ameliorating tumor penetration of the agents.[18] Therein, cell penetrating peptides (CPP) have appeared as an exciting candidate to decorate the nanoparticles, which have been proved to enhance intracellular delivery and tumor penetration of the agents.[24,25] However, due to the positive surface charge, these CPP modified nanosystem are sensitive to nonspecific phagocytosis of the reticuloendothelial system and easily adsorb the plasma proteins once injected into the blood, masking their long circulation in blood and targeting capacity to tumor sites, thereby critically influencing the in vivo biological fate and therapeutic effects.[26] The nanosystem decorated with poly (ethylene glycol) (PEG) and negative or neutral surface charge is considered to achieve long-term circulation in the blood and targeting capacity to tumor sites, however pouring their tumor penetration.[27] To address these limitations, nanosystem rational designed with efficient tumor targeting and penetrating capability is necessary to achieve the synergistic effects of chemo-chemodynamic combination therapy.

Recent reports have revealed that Nine D-arginine (r9), a superlative CPP, can effectively endow the nanosystem with penetrating capability to the tumor site.[28,29] Meanwhile, RGD peptide modification may specifically recognize highly expressed $\alpha v\beta_{3/5}$ integrins in tumor vessels or cancer cells to enhance tumor targeting.[30,31] In our previous results, we demonstrated the crucial role of the r9 peptide in strengthening the tumor penetration of the nanosystem and a cyclic CRGDfK peptide in enhancing the tumor targeting of nanoparticles.[32,33] Rationally, a re-constructed nanosystem decorated with a cyclic CRGDfK and r9 peptide can be an encouraging nanoplatform with tumor-targeting and deep tumor-penetration for effective chemo-chemodynamic combination therapy. In addition, pH-sensitive polymers are more attractive for targeted drug delivery owing to the different pH values of normal and tumor tissues. Most tumor tissues are extracellularly acidic, with a pH value lower than 7.4.[34] Upon delivering from normal tissue to extracellular tumor tissue (pH6.5), pH-responsive polymers undergo structural transition, followed by encapsulated drug release or the surface structure of the nanosystem changing.[35–37]

With this in mind, we describe a pH-sensitive mitoxantrone (MTO) and copper ion-loaded nanosystem functionalized with cyclic CRGDfK and r9 peptide (denoted as TPRN-CM) for chemo-chemodynamic combination therapy for metastatic breast cancer (Scheme 1). MTO and copper ions is respectively selected as the agents for chemotherapy and CDT of breast cancer.The cyclic CRGDfK peptide is linked with amphiphilic block copolymers composted of poly (β-amino ester) (PAE) and hydrophilic PEG (PAE-PEG_{5K}) which is designed to exhibit a sharp structure transition at extracellular acidic tumor environments (pH6.5). The r9 peptide was linked to distearoyl phosphoethanolamine (DSPE)-PEG_{2k} to form an amphiphilic peptide derivative (DSPE-PEG_{2K}-r9). As shown in Scheme 1, TPRN-CM would be quiescent in the blood circulation with the CRGDfK peptide on the surface of the nanoparticle to improve its targeting capacity to the tumor site. Then, PAE with tertiary amine that has a week basic character is protonated to transform into a hydrophilic polymer. As a result, the r9 peptide can be exposed to reverse the TPRN-CM surface charge in the acidic tumor microenvironment to promote deep penetration into tumor tissue and facilitate their internalization by cancer cells.

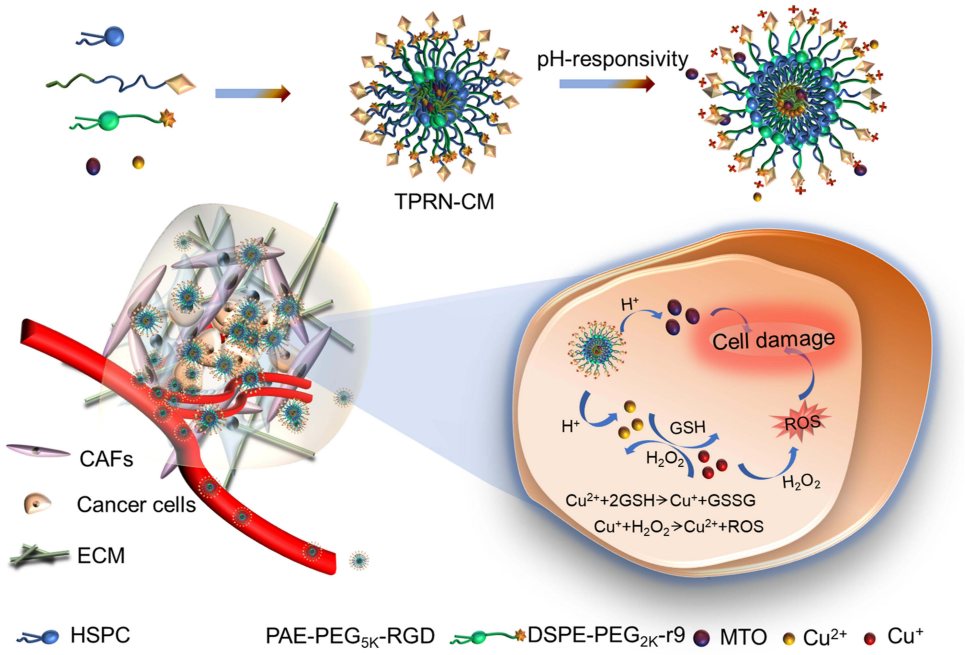

Scheme 1 Schematic illustration of pH-responsive charge-reversal TPRN-CM in acidic tumor microenvironment and the corresponding the mechanism of breast cancer chemo-chemodynamic combination therapy.

In this study, the rationality of this design for programmed targeting of breast cancer cells was validated by in vitro and in vivo evaluation. The nanosystem was decorated with PEG and a neutral surface charge to achieve long-term circulation in the blood and targeting capacity to tumor sites, followed by exposure of the positively charged CPP at the tumor site to penetrate the tumor tissue. Such structural changes in the nanosystem between normal and tumor tissues will facilitate the synergistic effects of chemo-chemodynamic combination therapy in breast cancer.

Material and Methods

Materials

Mitoxantrone (MTO), $CuCl_2 \cdot H_2O$, methylene blue (MB), 5.5'-Dithiobis- (2-nitrobenzoic acid) (DTNB), and L-glutathione (GSH) were obtained from Shanghai Macklin Biochemical Co. Ltd. DCFH-DA was purchased from Shanghai Beyotime Biotechnology Co. Ltd. Hydrogenated soybean phosphatidylcholine (HSPC), cholesterol, and DSPE-PEG_{2K} were supplied by Shanghai Advanced Vehicle Technology Pharmaceutical Ltd. The pH-sensitive amphiphilic block polymers PAE-PEG_{5K}-RGD, PAE-PEG_{5K}, and DSPE-PEG_{2K}-r9 were purchased from Xi'an Ruixi Biological Technology Co. Ltd. RPMI 1640 medium, Dulbecco's modified Eagle's medium (DMEM), fetal bovine serum (FBS), and calf bovine serum (CBS) were purchased from GIBCO, CA, USA).

Cell Lines and Animals

Murine metastatic 4T1 breast cancer cells and mouse NIH3T3 embryonic fibroblast cell were obtained from the Shanghai Cell Bank, Chinese Academy of Sciences (CAS). The 4T1 and NIH3T3 cells were respectively cultured in the RPMI 1640 medium supplemented with 10% FBS and, DMEM supplemented with 10% CBS, 100 U/mL of penicillin, and 100 μg/mL of streptomycin at 37 °C and 5% CO_2 in a humidified incubator. Meanwhile NIH3T3 cells were pre-activated with 10 ng/mL transforming growth factor-β (TGF-β) to differentiate into cancer-associated fibroblasts (CAFs).[38]

Female Kunming mice (18~22g) were provided by Guangdong Medical Laboratory Animal Center (GMLAS, Guangdong, China). All animal experiments were performed in accordance with experimental guidelines approved by the Institutional Animal Care and Use Committee (IACUC) of GMLAS, China.

Preparation and Characterization of MTO and Cu2+ Coloaded Nanoparticles (TPRN-CM)

The TPRN-CM nanoparticles was composed of MTO, Cu^{2+}, DSPE-PEG_{2k}-r9, PAE-PEG_{5k}-RGD, HSPC, and cholesterol (weight ratio: 1:0.08:1.5:2:10:2). First, DSPE-PEG_{2k}-r9, PAE-PEG_{5k}-RGD, HSPC, and cholesterol were dissolved in a solution of chloroform/methanol (v/v=1:1) in a round flask and evaporated to dryness under reduced pressure to form a thin film. The film was then dispersed in PBS (pH7.4) containing 0.1 M $CuCl_2{\cdot}H_2O$ and sonicated with a probe in a water bath for 5 min, followed by dialysis for 5 h to prepare a liposomal formulation (TPRN-C). Finally, the TPRN-C was incubated with MTO at 60 °C for 20 min to obtain the MTO and Cu^{2+}-co-loaded nanoparticles (TPRN-CM). In contrast, counterpart formulations of PRN-CM containing PAE-PEG_{5k} instead of PAE-PEG_{5k}-RGD and TPN-CM containing DSPE-PEG_{2k} instead of DSPE-PEG_{2k}-r9 were prepared using the same procedure.

To determine the pH-responsiveness of TPRN-CM, the particle size distribution and ξ potential of TPRN-CM in PBS (pH 7.4) and PBS (pH 6.5) were measured using dynamic light scattering (DLS; Nanoplus-3, Micromeritics). The morphology of TPRN-CM in PBS (pH 7.4) and PBS (pH 6.5) was determined using transmission electron microscopy (TEM, Tecnai G2 F20 S-Twin, FEI) after negative staining with uranyl acetate.

The encapsulation efficiency (EE) of MTO and Cu^{2+} in the nanosystem was determined. Unentrapped MTO and Cu^{2+} were separated from these nanoformulations by gel filtration using a Sephadex G-75. The MTO content was determined using UV-vis absorption spectrum analysis (Epoch, Biotek, USA) at a detection wavelength of 610 nm. The amount of Cu^{2+} entrapped in the TPRN-CM was analyzed using the flame atomic absorption spectrum method (AA-7000, Shimadzu, Japan) equipped with a hollow copper cathode lamp. The encapsulation efficiency (EE)was determined as the ratio of the amount of encapsulated drug to the total amount in the formulation. The measurements were performed in triplicate.

To evaluate the pH-responsive drug release profiles, TPRN-CM was incubated with PBS at pH 7.4 and pH 6.5, respectively, and then incubated at 37 °C for 12 h. The accumulated amounts of MTO and Cu^{2+} released at certain time intervals were analyzed using the aforementioned method. To evaluate the stability over time, the nanoformulations (TPRN-C, TPRN-M, TPRN-CM, TPN-CM, and PRN-CM) were incubated with PBS (pH 7.4) and FBS for 24 h. The EE of MTO and Cu^{2+} in the nanosystem at certain time intervals of incubation was successively determined by UV-vis absorption spectrum and flame atomic absorption spectrum analysis.

The GSH Consumption and ROS Generation of the TPRN-CM

GSH consumption and ROS generation in TPRN-CM were monitored. GSH solution (5 mM, 0.1 mL) was added to the TPRN-CM solution in PBS (pH 6.5) with serial concentrations of Cu^{2+} (0, 2.5, 5, 10, and 20 μg/mL, 0.85 mL) and maintained at room temperature with stirring for 30 min. Then, the DTNB solution (3.0 mg/mL, 0.05 mL) was added, and the mixtures were incubated for another 30 min. The remaining amount of GSH was determined by measuring absorbance at 412 nm. Moreover, the GSH solution (5 mM, 0.1 mL) was added to TPRN-CM nanoparticle solution at 10 μg /mL of Cu^{2+} (0.85 mL), maintained at 25 °C under stirring for given intervals (0, 15, 30, 60, 120 min).Then, DTNB solution (3.0 mg/mL, 0.05 mL) was added, and the remaining amount of GSH was obtained by measuring the absorbance at 412 nm. The background solution consisted of a mixed solution of TPRN-CM and DTNB.

In addition, the production of •OH radicals was investigated using methylene blue (MB) as a reliable indicator of MB degradation after reacting with the •OH radical and showing an absorbance change at 665 nm. Hence, TPRN-CM was mixed with different GSH concentrations (0, 0.5, 2.5, 5, and 10 mm) at pH 6.5, and 10 mg/mL MB and 10 mm H_2O_2 were added to this solution. After 30 min of reaction in the dark, the absorbance spectra of the reaction solution from 500 nm to 800 nm at 10 nm intervals were measured by UV-vis absorption spectrum analysis at room temperature. TPRN-CM was then mixed with 5 mm GSH at different pH values (pH 6.5 and pH 7.4) and 10 mg/mL MB and 10 mm H_2O_2 were added. After 30 min of reaction in the dark, the reaction solution was analyzed using the above method.

Cellular Uptake

The uptake of the nanosystems, including TPRN-CM, TPN-CM, and PRN-CM at pH 7.4 or pH 6.5 in 4T1 cells was visualized under an inverted fluorescence microscope (IX73, Olympus, Japan). Sterile round glass coverslips were placed in a 24-well plate before the cells were seeded at 1×10^4 cells/well. After 24 h, the nanosystem was added to each well at 1 μg/mL MTO and incubated for 4 h. The cells were then stained with Hoechst 33342 (Blue, Beyotime) for visualization under an inverted fluorescence microscope. Cellular uptake of the nanosystem was quantified by flow cytometry (CytoFlex, Beckman, USA). Cells were seeded into 12-well culture plates at 2×10^5 cells per well, cultured overnight, and then incubated with TPRN-CM, TPN-CM, and PRN-CM at 1 μg/mL of MTO at pH 7.4 or pH 6.5. 4T1 cells treated with saline were used as negative controls. After 4 h, the cells were harvested and the mean fluorescence intensity of each sample was determined by flow cytometry. All experiments were performed in triplicates.

Tumor Penetration of TPRN-CM in vitro

In vitro tumor penetration of TPRN-CM was determined using transwell-mediated assays. In order To simulate the microenvironment of tumor tissue in vitro, the top chamber of inserts (24-well, pore size, 8 μm, Costar) was coated with 60 μL of Matrigel (Beyotime, China) diluted in serum-free medium and then placed in a 37 °C incubator for 30 min. Activated NIH3T3 and 4T1 cells were seeded into the upper and lower chambers, respectively. After 24 h of incubation, the nanosystem (TPRN-CM (pH 7.4, pH 6.5), PRN-CM, and TPN-CM) was added to the upper chambers of the inserts at 1 μg/mL MTO. After 4h, 4T1 cells in the lower chamber were harvested, and the mean fluorescence intensity in each sample was determined by flow cytometry. All experiments were performed in triplicates. Drug-free 1.1'-dioctadecyl-3,3,3',3'-tetramethylindodicarbocyanine (DiD)-loaded TPRN (TPRN-D) was used to confirm the reliability of the Transwell chamber model.

Chemodynamic Activities of TPRN-CM in 4T1 Cancer Cells

To determine the chemodynamic activity of TPRN-CM in 4T1 cancer cells, 2',7'-dichlorodihydrofluorescein diacetate (DCFH-DA, 10μM) was used as a ROS probe to detect intracellular ROS in 4T1 cells. Cells were seeded into 12-well plates at a density of 8×10^4 cells per well and incubated for 12 h. Then. The cells were stained with DCFH-DA (1.7 μL, 10 μM in serum-free medium) at 37 °C. After 30 min of co-culture, the medium was replaced with fresh complete medium containing PBS, Cu^{2+}, TPRN-C (pH 6.5 and pH 7.4), PRN-C (pH 7.4), and TPN-C (pH 7.4) at 0.08 μg/mL a Cu^{2+} concentration of 4h. The cells were then washed with serum-free 1640 and digested into single cells for flow cytometry. All experiments were performed in triplicates.

Cytotoxicity

The cytotoxicity of TPRN-CM was measured in 4T1 cancer cells. Briefly, cells were seeded into 96 well plates at a density of 3×10^3 cells per well and cultured overnight. MTO, TPRN-C, TPRN-M, TPRN-CM (pH 7.4, 6.5), PRN-CM, and TPN-CM were added to each well at serial concentrations of MTO (0.1, 0.625, 1.25, 2.5, 5, and 10 μg/mL) or equivalent concentrations. After 48 h of incubation, cell viability in each group was detected using thiazolyl blue tetrazolium bromide (MTT, Sigma) assays. All samples were analyzed in triplicate.

Inhibitory Effects on Cell Migration and Invasion Activities

The inhibitory effect of TPRN-CM on cell migration and invasion was determined using transwell assays. For the cell migration assay, 4T1 cells in 200 μL serum-free medium were seeded into the top chamber of inserts (24-well, pore size, 8 μm, Costar) at 2×10^5 cells per well. For the cell invasion assay, 60 μL of Matrigel (Beyotime, China) diluted in serum-free medium was added to the inserts and incubated for 30 min before 200 μL of serum-free medium was added to the inserts at 2×10^5 cells per well. Next, 600 μL of culture medium containing 10% FBS was added to the well of 24-plate. Nanosystems (MTO, TPRN-C, TPRN-M, TPRN-CM (pH 7.4, pH 6.5), PRN-CM, and TPN-CM) were added to the upper chambers of the inserts at 100 ng/mL or equivalent concentrations of MTO. Saline-treated cells were used as negative controls. After 24 h, the cells that migrated or invaded across the membrane were stained with crystal violet and imaged under a microscope (IX73, Olympus, Japan) to evaluate their inhibitory effects on cell migration and invasion. The crystal violet signals for each treatment were analyzed using the ImageJ software (National Institutes of Health, Bethesda, USA).

Vitro Growth Inhibition of Tumor Spheroids

Three-dimensional (3D) tumor spheroids were used to further evaluate the growth inhibition of the nanosystem in vitro. Briefly, 100 μL of suspensions of 4T1 cells was cultured in a 1% (wt/vol) agarose gel-coated 96-well plate at 1×10^3 cells per well.[39] After 3 days, MTO, TPRN-C, TPRN-M, TPRN-CM (pH 7.4, pH 6.5), PRN-CM, and TPN-CM were added to the plates at 1 μg/mL of MTO or equivalent concentration. Untreated tumor spheroids were used as negative controls. The day of administration was considered day 0, and spheroid growth was monitored for 6 days using a microscope (IX73, Olympus, Japan).The tumor spheroids volume on day 0 and 6 was quantified by the formula $V=L\times W^2/2$ (L, the longest dimension; W, the shortest dimension). The tumor spheroids volume at Day 6 compared to Day 0 treatment represented for the inhibitory effects on the spheroids growth of each treatment.

Tumor Penetration of TPRN-CM

The penetration of TPRN-CM into the tumor mass was also measured. The Tumor tissues from TPRN-CM- and TPN-CM-treated groups were collected at 8 h after injection, embedded in the optimal cutting temperature compound, frozen at 20 °C for sectioning at 10 μm. The tumor sections were fixed with 4% paraformaldehyde and stained with 40.6-diamidino-2-phenylindole (DAPI, blue, Beyotime) and actin-tracker green (green, Beyotime) for visualization under a confocal laser scanning microscope (CLSM, TCS-SP8 STED, Leica, Germany). Finally, fluorescent signals from the entire tumor mass were collected to provide a complete view. The fluorescence signals of MTO in each treatment were analyzed using ImageJ software (National Institutes of Health, Bethesda, USA).

In vivo Therapeutic Effects of TPRN-CM-Mediated Chemo-Chemodynamic Therapy

First, a tumor model was established by subcutaneous injection of 4T1 cells at 1×10^6 cells per mouse. When the tumor volume reached approximately 150 mm^3, mice were randomly divided into seven groups (n=6) and treated with PBS, MTO, TPRN-C, TPRN-M, TPRN-CM, PRN-CM, or TPN-CM at 5 mg/kg of MTO or 0.4 mg/kg of Cu^{2+} via tail injection, respectively. The treatments were repeated for a total of four times. Body weight and tumor volume were monitored at certain time intervals. The tumor volume was quantified by the formula $V=L\times W^2/2$ (L,the longest dimension; W, the shortest dimension). The tumor growth index (TGI) of each treatment was calculated as the tumor volume at certain time points compared to the initial time of drug treatment, and was used to evaluate the inhibitory effects on tumor growth.[40] On day 21 after the first treatment, tumor size was measured to calculate the TGI values for each treatment. The major organs, including the heart, liver, spleen, lung, kidney, and tumor tissues, from each group were carefully collected. Tumor tissue was photographed and weighed to determine its inhibitory effect on tumor growth. The number of visually detected metastatic nodules in the lungs of each group was recorded. Finally, the collected major organ tissues were fixed in 4% formalin solution, embedded in paraffin, and sectioned at 5 μm for histological studies using hematoxylin and eosin (H&E) staining. In addition, the tumor sections were analyzed using the terminal deoxynucleotidyl transferase dUTP nick-end labeling (TUNEL) assay kit (green, Roche, USA) to investigate the apoptosis of cancer cells in a tumor.

Statistical Analysis

Data are expressed as means ±standard deviation (SD). Statistical analysis between two groups was performed using a two-tailed Student's *t*-test. Differences were considered significant when the *P* value was less than 0.05.

Results and Discussion

Characterization of TPRN-CM

In this study, TPRN-CM nanoparticles consisted of MTO, copper ions, DSPE-PEG_{2k}-r9, PAE-PEG_{5k}-RGD, HSPC, and cholesterol. In this nanosystem, HSPC and cholesterol were used as the major constituents to construct a liposome system. The cyclic CRGDfK peptide in PAE-PEG_{5k}-RGD may specifically recognize highly expressed $\alpha v\beta_{3/5}$ integrins in tumor vessels or cancer cells to endow the system with tumor-targeting ability.[30] The r9 peptide in DSPE-PEG2k-r9 could penetrate the cell membrane to endow the nanoparticles with tumor penetration.[28] The PAE-PEG5k-RGD in the TPRN-CM could cover the r9

peptide in blood circulation and be protonated to change the structure of the nanoparticle to expose the r9 in the acidic tumor microenvironment. MTO is a cytotoxic agent that can efficiently inhibit the synthesis of DNA strands to inhibit cell proliferation for anticancer therapy.[41] Copper ions (Cu^{2+}) can be reduced to Cu^{+} under a high concentration of L-glutathione (GSH) in tumor site to further efficiently trigger the Fenton-like reaction to convert H_2O_2 into highly toxic • OH-mediated CDT,[42,43] and chelate with MTO to prevent premature leakage in the carrier. In this study, both MTO and copper ions were loaded into TPRN-CM nanoparticles to realize their effective delivery to solid tumors for chemo-chemodynamic combination therapy. Meanwhile, a counterpart liposome formulation without MTO, copper ions, DSPE-PEG_{2k}-r9, or PAE-PEG_{5k}-RGD was prepared as a control and named TPRN-C, TPRN-M, TPN-CM, or PRN-CM, respectively.

The morphologies of TPRN-CM in phosphate buffered solution(PBS) (pH 7.4) or PBS (pH 6.5) were visualized using TEM, which showed nanometer-sized spherical particles. Dynamic light scattering (DLS) analysis revealed that the hydrodynamic diameter was 127.6±9.3 nm (polydispersity index, PDI, 0.20±0.05) for TPRN-CM in PBS (pH 7.4), and 195.4±14.1 nm (PDI, 0.13±0.06) in PBS (pH 6.5) (Figure 1A and B). The ξ potential values were as follows:

-24.0±1.6 mV for TPRN-CM in PBS (pH 7.4) and 10.3±3.7 mV in PBS (pH 6.5)(Figure 1C). In addition, the mean diameter and ξ potential values of TPRN-C, TPRN-M, TPN-CM, and PRN-CM were also analyzed at pH 7.4 or pH 6.5 (Table S1). Because of the pH-sensitive property of the PAE polymer, the nanoparticles with DSPE-PEG_{2k}-r9 would

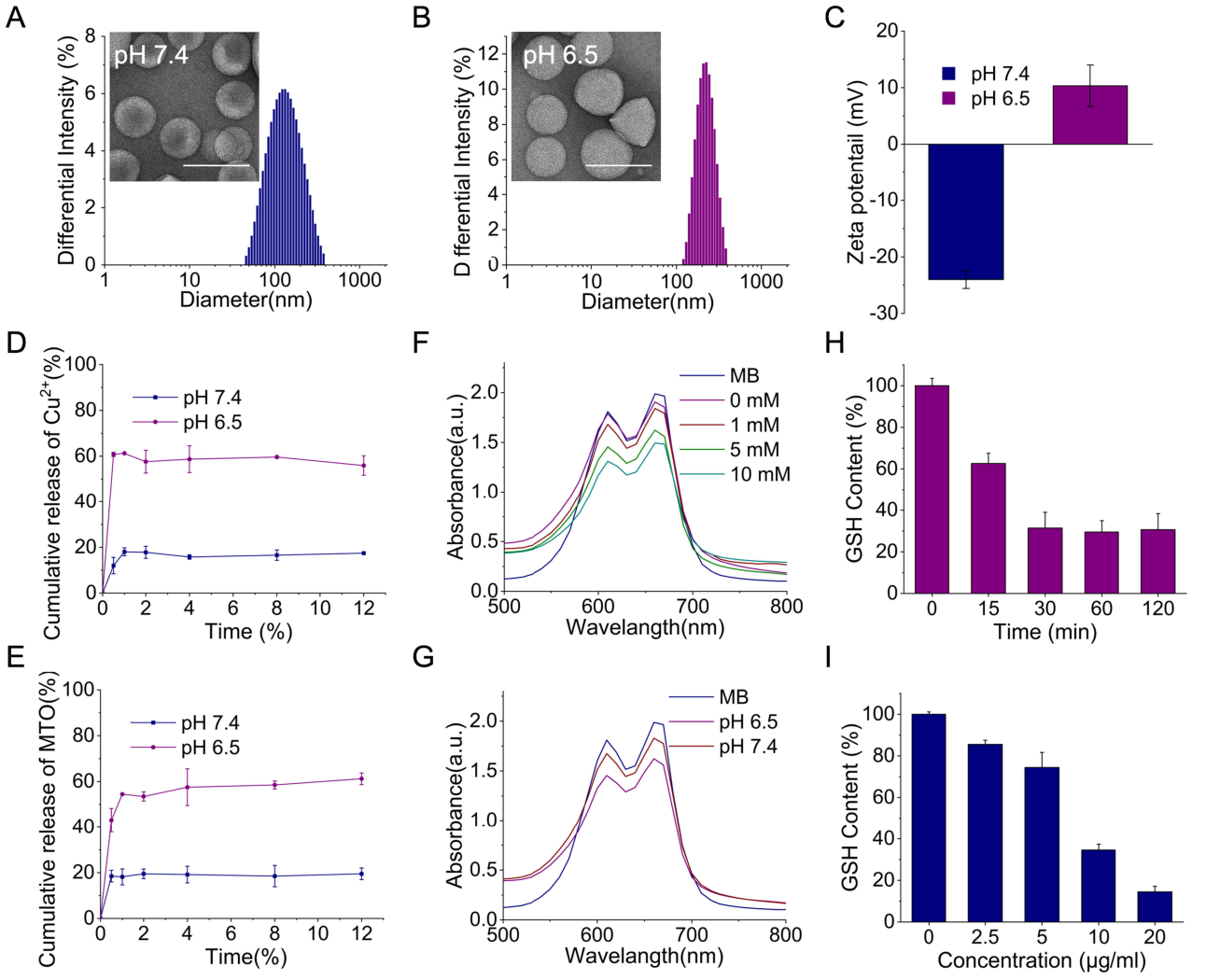

Figure 1 Characterization, ROS production and GSH consumption Of TPRN-CM. (**A** and **B**) Hydrodynamic size, TEM images (scale bar=200 nm) and (**C**) Zeta potential of TPRN-CM in pH 7.4 or 6.5. (**D**) Copper ions and (**E**) MTO release profiles of TPRN-CM at different pH with increasing time (n=3). (**F**) MB degradation by ·OH after treatment of TPRN-CM, H_2O_2, MB with different concentration of GSH in pH 6.5, and (**G**) MB degradation with 5 mM GSH in pH 6.5 or pH 7.4. (**H**) Concentration-dependent and (**I**) Time-dependent GSH consumption by TPRN-CM (n=3), respectively.

swell in PBS (pH 6.5) to expose the r9 peptide, further causing charge reversal, which could enhance the tumor penetration of the drugs.[44,45]

Next, we measured the EE of MTO and copper ions in TPRN-CM, TPRN-M, TPRN-C, TPN-CM, and PRN-CM (Table S1). The EE of the nanosystem was also tested within 24 h when they were incubated with PBS (pH 7.4) or whole fetal bovine serum (FBS) (Figure S1 and S2). The measurement results indicated that the EE of MTO and copper ions in both co-loaded nanosystems barely changed after incubation with PBS (pH 7.4) or FBS, suggesting good stability over time in mimicked physiological environments. However, the EE of MTO in TPRN-M and copper ions in TPRN-C were significantly reduced. The good stability of TPRN-CM,TPN-CM, and PRN-CM could be due to the interactions between MTO and copper ions in the nanosystem. The good stability of the system and high EE of the drug in both the MTO and copper ion-co-loaded nanosystems could provide an essential prerequisite for combinational chemo-chemodynamic therapy and suggest fewer side effects or additive effects compared to TPRN-M.

The in vitro release profiles of MTO and Cu ions from TPRN-CM were investigated in PBS at different pH values, and the results indicated that they were released in a pH-responsive manner (Figure 1D and 1E). PAE (poly(β-amino ester)) has a week basic character because of its tertiary amine and can be protonated at a low pH, resulting transform the PAE-PEG_{5K}-RGD from an amphiphilic molecule to a hydrophilic. Finally, the TPRN-CM would swell to release drug in acidic pH. The accumulated release of MTO and copper ions in PBS at pH 6.5. rapidly increased to approximately 60% within 4 h, which was much higher than that at pH 7.4. The in vitro release profiles indicated that TPRN-CM would be stable in the blood circulation and responsively release MTO and copper ions in a weakly acidic tumor microenvironment (pH 6.5), which could be beneficial for producing therapeutic effects.

The GSH Consumption and ROS Generation Ability of TPRN-CM

Several studies have demonstrated that the copper ions (Cu^{2+}) can be reduced to Cu^{+} under a high concentration of L-glutathione (GSH), which results in the consumption of GSH via transformation into oxidized GSH.[43] The Cu+ can further efficiently catalyze H_2O_2 into •OH radical via Fenton-like reactions to mediate CDT.[43,46] The high expression of GSH and H_2O_2 in the tumor microenvironment provides powerful conditions for CDT of Cu^{2+}. Ellman's test was performed to evaluate GSH consumption.[47] Our findings revealed that TPRN-CM could effectively consume GSH because of the satisfactory redox cycling of Cu ions (Figure 1H and 1I). The generation of toxic free radicals affects the anti-tumor effects of TPRN-CM. The production of •OH radicals was investigated using methylene blue (MB) as a reliable indicator of MB degradation after reacting with the •OH radical and showing the absorbance change at 665 nm.[48] TPRN-CM, H_2O_2, and MB were added to PBS (pH 6.5) with different concentrations of GSH to simulate the response. According to the absorbance curve shown in Figure 1F, TPRN-CM can trigger the gradual degradation of MB with an increase in GSH concentration from 0 to 10 mm, demonstrating the occurrence of a cascade reaction of TPRN-CM with GSH and H_2O_2 to generate •OH. TPRN-CM was added to PBS (pH 6.5) or PBS (pH 7.4) containing H_2O_2, MB, or GSH (5 mM). As shown in Figure 1G, the nanosystem in PBS (pH 6.5) stimulated the degradation of MB more effectively than that in PBS (pH 7.4), suggesting that an acidic environment was beneficial for the CDT of TPRN-CM. These findings confirm that TPRN-CM can generate •OH radicals for chemodynamic therapy via the Fenton catalytic process in the TME.

In vitro Cellular Uptake of TPRN-CM

Cellular uptake of TPRN-CM, TPN-CM, and PRN-CM in PBS (pH 7.4) or PBS (pH 6.5) was determined in 4T1 cancer cells using an inverted fluorescence microscope and flow cytometry analysis, wherein MTO was used as a fluorescence dye for the measurements. The captured images showed that all nanosystems could be extensively internalized into the 4T1 cancer cells (Figure 2A). The flow cytometer results showed that the cellular uptake of TPRN-CM was significantly higher than that of PRN-CM in 4T1 cancer cells in PBS (pH 7.4) (Figure 2B), there is no difference between TPRN-CM and TPN-CM. Compared with PRN-CM, the cyclic CRGDfK peptide in the TPRN-CM and TPN-CM systems promotes its binding to $\alpha v\beta_{3/5}$ integrins on cancer cells, thereby enhancing their internalization by cancer cells. According to the flow cytometry results shown in Figure 2C, in the TPRN-CM and PRN-CM groups, cellular uptake in PBS (pH 6.5) was significantly higher than that in PBS (pH 7.4) in 4T1 cancer cells, owing to the r9 peptide of TPRN-CM and PRN-CM

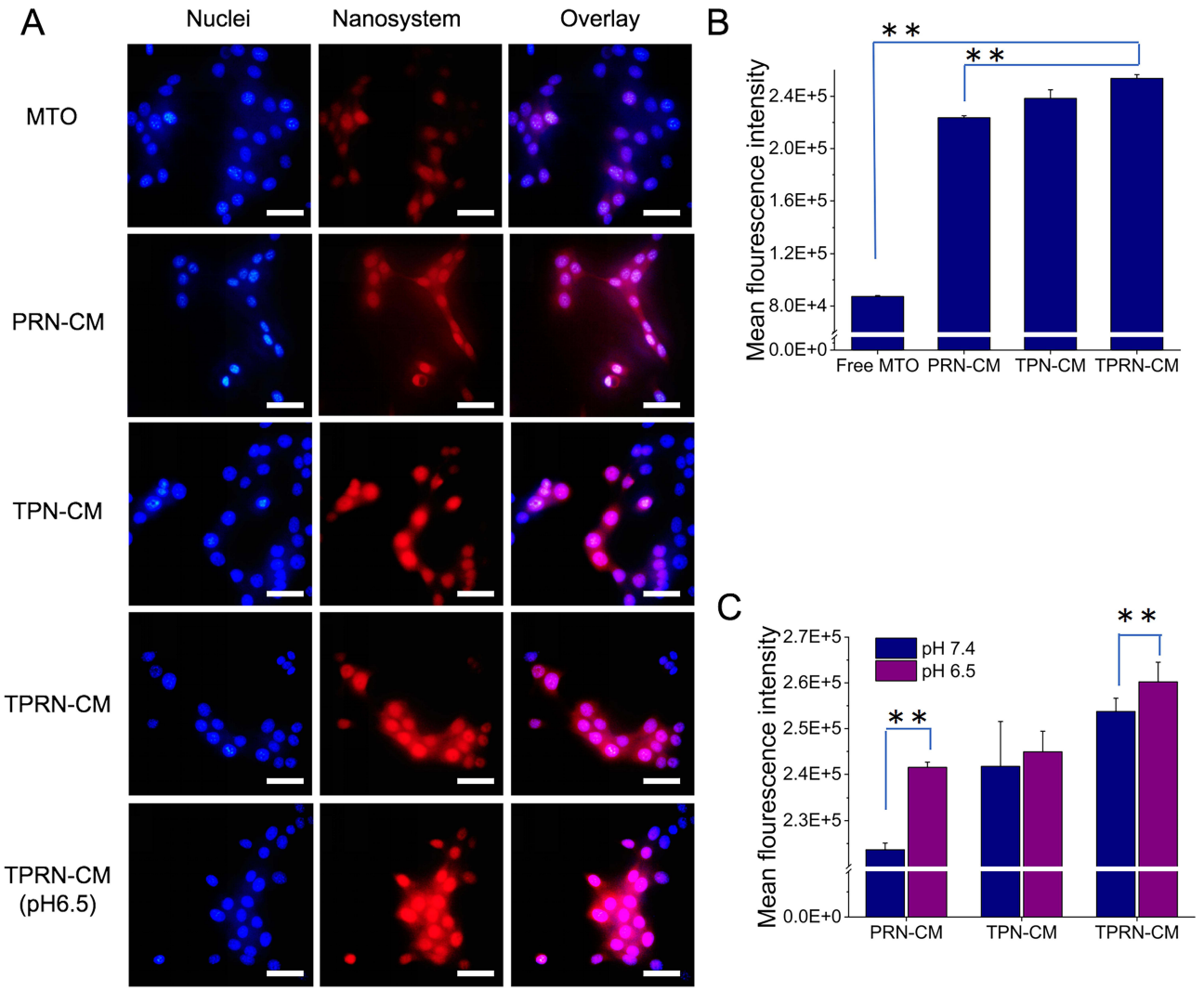

Figure 2 Cellular uptake of TPRN-CM in 4T1 cells. (**A**) Typical images of cellular uptake of nanoparticles under the inverted fluorescence microscope, scale bar=25 μm. (**B**) The internalization of the various nanoparticles in 4T1 cells in pH 7.4, and (**C**) the internalization in pH 6.5 and pH 7.4. Data are mean±SD (n=3). $^{**}P<0.01$.

being exposed to PBS (pH 6.5) to promote their internalization by cancer cells. The cyclic CRGDfK peptide can make TPRN-CM more easily recognized by tumor cells, while the r9 peptide can help TPRN-CM penetrate the cell membrane, ultimately leading to preferential uptake of TPRN-CM in 4T1 cancer cells in the TME.

In vitro Specific Tumor Penetration of TPRN-CM

To verify the penetrating capacity of the nanosystem, a Transwell chamber model was used to assess its ability to overcome biological barriers. In this model, activated NIH3T3 cells and Matrigel were used to simulate SCs and ECM, respectively, in the tumor tissue. As shown in Figure 3A, different cells were seeded in different chambers of the insets to form a biological barrier, and nanosystems (TPRN-D (pH 7.4, 6.5), TPRN-CM (pH 7.4, 6.5), PRN-CM, and TPN-CM) were added to the top chamber. The fluorescence intensity of DiD or MTO in the bottom chamber of 4T1 cells was analyzed by flow cytometry (Figure 3B and C). In the treatment groups, TPN-CM and TPRN-CM specifically recognized 4T1 and damaged CAFs at pH 7.4. The PRN-CM nanosystem could damage CAFs at pH 7.4. The TPRN-CM nanosystem can recognize 4T1, damage CAFs, and penetrate membranes at a pH of 6.5.

Before evaluating the penetration function of the nanosystem, we prepared drug-free TPRN-D to evaluate whether the Transwell model could simulate different barriers. As shown in Figure 3B, the 4T1, 4T1+CAFs, 4T1+Matrigel, and 4T1 +Matrigel + CAFs groups showed no barriers, stromal cell capture, ECM trapping, stromal cell capture, and ECM

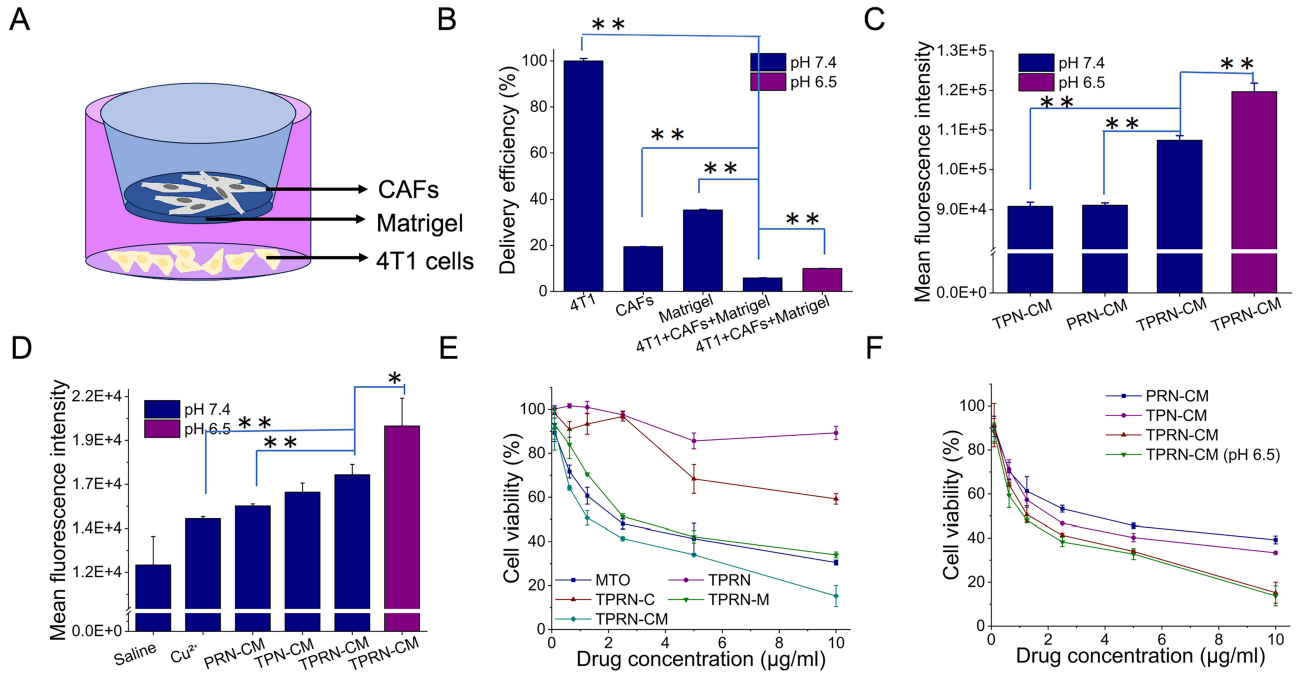

Figure 3 Penetration, ROS production, cytotoxicity of the nanocomplex in 4T1 cells in vitro. (**A**) The transwell chamber model. (**B** and **C**) The mean fluorescence intensity of nanocomplex after different treatments in 4T1 cells by flow cytometry, n=3. (**D**) Production of ROS in 4T1 cells treated with the various nanoparticles by flow cytometry, DCFH-DA was used as probe to monitor the ROS production. (**E**) Cytotoxicity of TPRN, TPRN-C, TPRN-M,TPRN-CM in 4T1 cells. (**F**) Cytotoxicity of TPRN-CM, TPN-CM, PRN-CM,TPRN-CM (pH 6.5) in 4T1 cells. Data are mean±SD (n=3). $^{*}P<0.05$, $^{**}P<0.01$.

trapping, respectively. The drug-free TPRN-D in the 4T1 group showed 100% delivery efficiency. Our results showed that the presence of stromal cells (CAFs), ECM (Matrigel), combined stromal cells (CAFs) and ECM (Matrigel) decreased the delivery efficiency from 100% to 19.5%, 35.4%, and 5.8%, respectively. Therefore, the constructed Transwell model was suitable for determining the penetration ability of the nanosystem.

Based on the effectiveness of the transwell model, we evaluated whether these treatments could improve the poor delivery efficiency caused by the aforementioned barriers. As shown in Figure 3C, the TPRN-CM nanosystem in pH 6.5 significantly improved the the delivery efficiency comparing with TPRN-CM, PRN-CM and TPN-CM in pH 7.4, suggesting that TPRN-CM in pH 6.5 with the r9 peptide exposing possessed better penetrating function over the other groups. The considerable penetration function of TPRN-CM in vitro in PBS (pH 6.5) demonstrated its great potential for effective tumor penetration in vivo.

The ROS Generation Ability of TPRN-CM

Then, the 2', 7'-dichlorodihydrofluorescein diacetate (DCFH-DA) that could be oxidized into DCF (green fluorescence) by ROS was used as a intracellular ROS probe to detect the TPRN-C-mediated ROS generation in 4T1 cancer cells.[49] Due to fluorescence interference of MTO, the TPRN-C was applied to replace TPRN-CM to test the nanosystem-mediated ROS generation. As shown in Figure 3D, cells cultured with TPRN-C displayed significantly higher fluorescence than the other groups in PBS (pH 7.4). Notably, TPRN-C in PBS (pH 6.5) exhibited a significantly brighter fluorescence than TPRN-C in PBS (pH 7.4). Combining the cellular uptake results, we suggest that the cyclic CRGDfK peptide and r9 peptide of TPRN-C promote the preferential uptake of TPRN-C, further leading to increased ROS generation in 4T1 cancer cells.

The Therapeutic Effects of TPRN-CM in vitro

The cytotoxicity of TPRN-CM, TPRN-M, TPRN-C, and free MTO was investigated in 4T1 cells (Figure 3E). A blank nanosystem of TPRN-CM (denoted as TPRN) was used as a control. As shown in Figure 2C, TPRN-CM, TPRN-M, and free MTO significantly inhibited the viability of 4T1 cells in a concentration-dependent manner in PBS (pH 7.4), whereas

TPRN exhibited negligible inhibition. As shown in Figure S3A, the half maximal inhibitory concentration (IC_{50}) of TPRN-CM, TPRN-M, and free MTO was respectively 1.51±0.15 μg/mL, 3.52±0.07 μg/mL and 2.62±0.48 μg/mL. Significant differences were detected between TPRN-CM and TPRN-M, indicating that Cu^{2+} enhances the inhibitory effect of MTO. The cytotoxicity of TPRN-CM, PRN-CM, and TPN-CM in PBS (pH 7.4) and TPRN-CM in PBS (pH 6.5) was investigated in 4T1 cells. As shown in Figure 3F, all groups showed similar inhibition of 4T1 cell viability. Comparing the IC_{50} of the groups, there was a significant difference between TPRN-CM in PBS (pH 6.5) and other groups (Figure S3B). The inhibitory effects of TPRN-CM in PBS (pH 6.5) can be largely attributed to the membrane penetration activities of the r9 peptide and the specific recognition ability of the cyclic CRGDfK peptide. The considerable inhibition of 4T1 cells by TPRN-CM in PBS (pH 6.5) demonstrated great potential for effective anticancer therapy.

Transwell-mediated assays were performed to evaluate the inhibitory effects of TPRN-CM on migration and invasion of metastatic 4T1 cells (Figure 4). Cell migration and invasion are two key steps in cancer metastasis.[50] In Figure 3E, each treatment group at 100 ng/mL of MTO or equivalent concentrations showed high cell viability and did not impact the assays. TPRN-CM, PRN-CM, TPN-CM, TPRN-M, and MTO considerably inhibited the migration and invasion activities of 4T1 cells, whereas TPRN-C had no inhibitory effects (Figure 4A and C). Compared to the negative control, TPRN-CM treatment in PBS (pH 6.5) resulted in 93.4% inhibition of cell migration and 93.0% suppression of cell invasion, which was significantly higher than the other groups in PBS (pH 7.4) (Figure 4B–D).The excellent inhibitory activity of TPRN-CM in PBS (pH 6.5) is largely attributed to the specific recognition ability of the cyclic CRGDfK peptide, particularly the membrane penetration activity of the r9 peptide masked in pH 7.4.TPRN-CM considerably inhibited the migration and invasion of 4T1 cells in PBS (pH 6.5), demonstrating enormous potential for anti-tumor metastasis.

Growth Inhibition Within 3D Tumorsphere in vitro

Although the exciting results showed that TPRN-CM could effectively inhibit the viability of cancer cells in the 2D cell culture experiments mentioned above, conventional 2D cell culture could not completely mimic the unique conditions of tumor tissues. Therefore, we introduced 3D tumor spheroids to further examine the efficacy of the designed nanoparticles in vitro. The growth inhibitory effect of TPRN-CM on 3D spheroids is shown in Figure 5. Compared with the saline control group, the MTO-loaded nanodrugs displayed an inhibitory effect on spheroid growth. However, both the MTO and Cu^{2+}-co-loaded nanosystems exhibited smaller growth areas from the third day after administration, suggesting additive effects compared to the monotherapy. In addition, the tumor spheroids volume at Day 6 compared to the Day 0 treatment was calculated to represent the inhibitory effects on the spheroids growth of each treatment. Compared with day 0, on day 6 after administration, the tumor sphere growth of TPRN-CM at pH 6.5 was significantly reduced to 38.8%, while the tumor sphere growth of TPRN-CCM, TPN-CM, PRN-CM, TPRN-M, and MTO at pH 7.4 was 59.5%, 59.4%, 48.3%, 63.9%, and 64.5%, respectively. It can be seen that TPRN-CM treated in PBS (pH 6.5) has a greater inhibitory effect on tumor spheroid growth than other treatments in PBS (pH 7.4). This could be attributed to the rapid release of MTO and Cu^{2+}, and the membrane penetration activity of the r9 peptide in PBS (pH 6.5). Accordingly, the encouraging results of 2D cell culture and 3D spheroid experiments proved the efficacy of TPRN-CM in vitro, laying a solid foundation for in vivo experiments.

In vivo Specific Tumor Penetration of TPRN-CM

In contrast, tumor sections were stained with actin-tracker green (Beyotime, Jiangsu, China) and DAPI. In the captured images (Figure 6A), both TPRN-CM and TPN-CM were unevenly distributed throughout the entire tumor mass. The red fluorescence signals of TPRN-CM and TPN-CM were readily detected regardless of the edge or deep areas of the tumor tissue. TPRN-CM and TPN-CM aggregated in the tumor boundary region, mainly due to the relatively abundant distribution of tumor blood vessels and SCs at the solid tumor edge, which limited their delivery to the deep areas of the tumor.[20,51] Notably, the image analysis data showed that the red signals of TPRN-CM in the tumor mass could be observed more widely with stronger intensity than TPN-CM (Figure 6B). These results indicated that TPRN-CM and TPN-CM could permeate through the tumor mass, and TPRN-CM displayed a wider penetration with stronger intensity

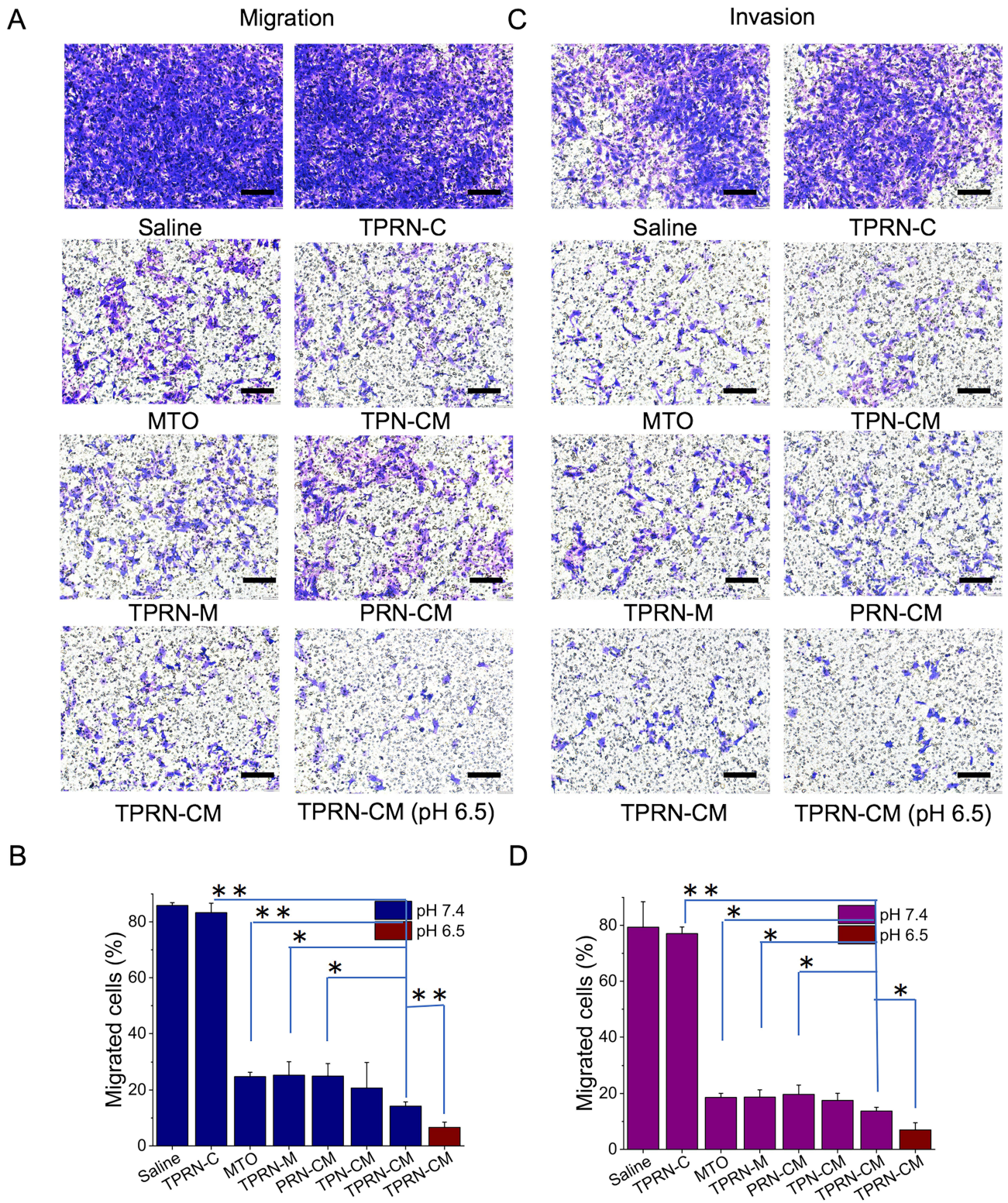

Figure 4 Inhibition of TPRN-CM on migration and invasion of 4T1 cells in vitro. (**A**) The typical images of migrated and (**C**) invaded cells across the transwell, scale bar=100 μm. (**B**)The percentage of migrated and (**D**) invaded cells compared to the negative control. Data are mean±SD (n=3). $^{*}P<0.05$, $^{**}P<0.01$.

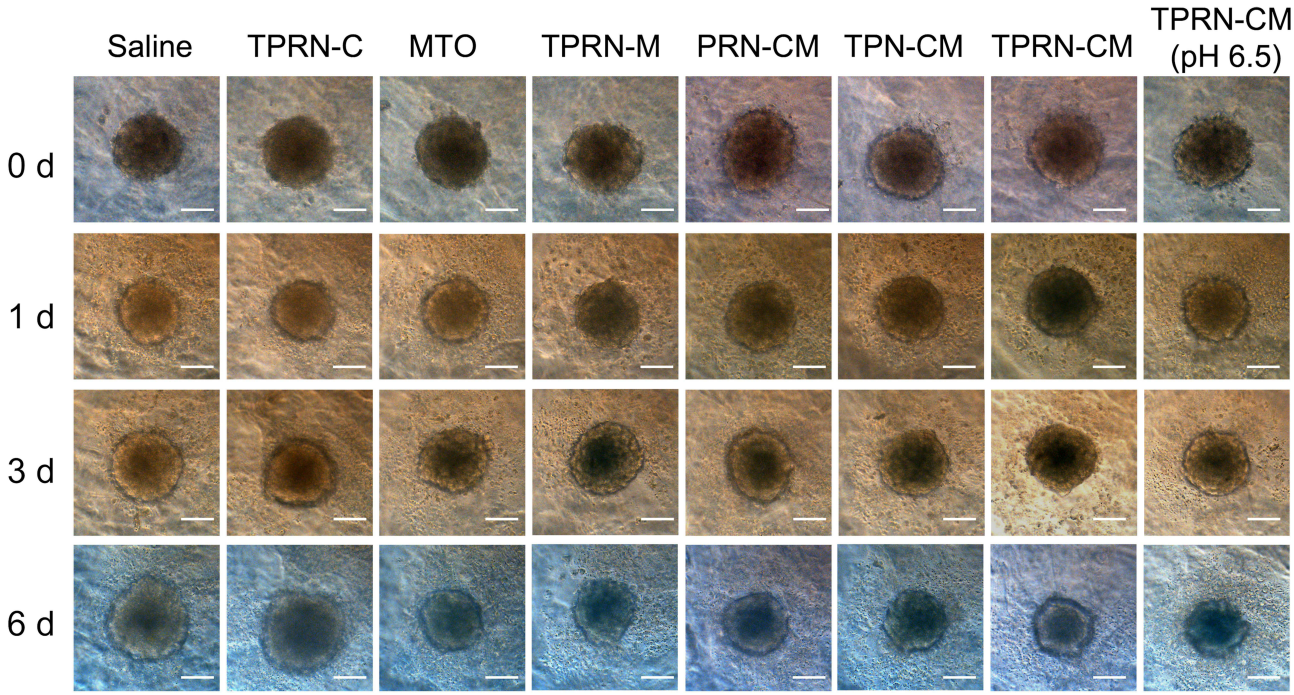

Figure 5 Representative images of 3D tumor spheroids after treatment with different nanoparticles, scale bar=100 μm.

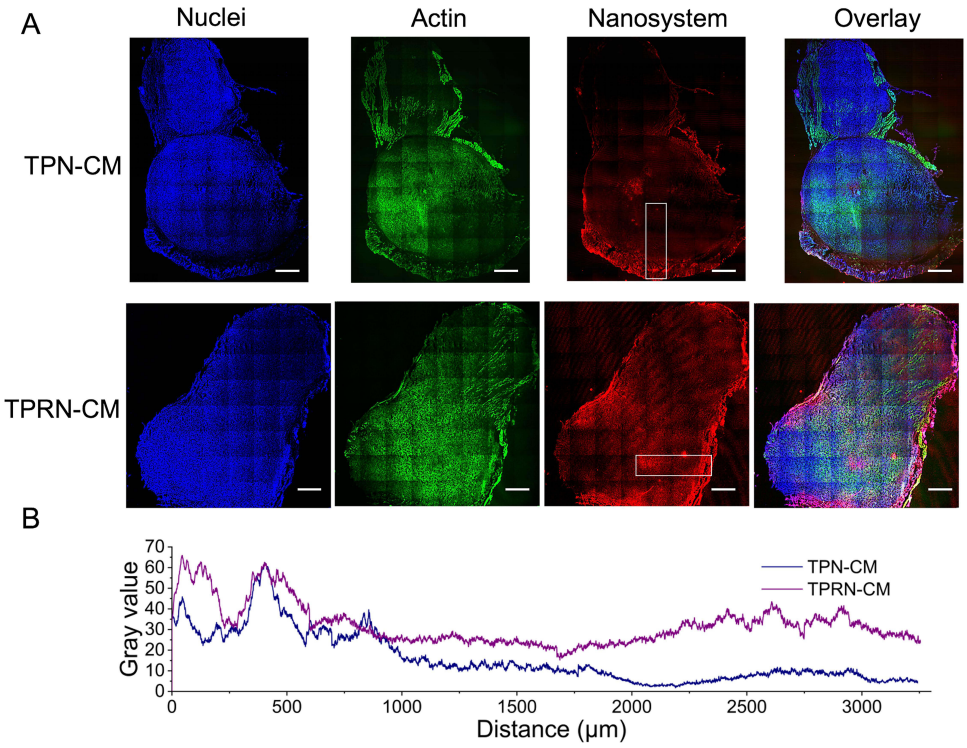

Figure 6 The penetration of TPRN-CM in tumor mass. (**A**) The intratumoral penetration of TPN-CM and TPRN-CM throughout the tumor mass measured by CLSM examination. Tumor sections were stained with DAPI and Actin-Tracker green for visualization, scale bar = 1 mm. (**B**) The diffusion of BL-D and BL-RD in tumor mass from exterior to interior regions quantified by Image J software.

https://doi.org/10.2147/IJN.S479125 DovePress

than TPN-CM due to the exposure of the r9 peptide in the weakly acidic tumor microenvironment. As a result, the considerable penetration of TPRN-CM into tumor tissues demonstrates great potential for effective anticancer therapy.

In vivo Anti-Tumor Therapy of TPRN-CM

The therapeutic effect of TPRN-CM-mediated combination therapy on tumor growth was evaluated in a 4T1-induced tumor model (Figure 7). When tumor volume reached approximately 150 mm^3, mice were respectively injected with saline, free MTO, TPRN-C, TPRN-M, TPRN-CM, TPN-CM, PRN-CM at 5 mg/kg of MTO and 0.4 mg/kg of Cu^{2+} for a total of 4 times (Figure 7A). Tumor growth and body weight were monitored during the treatment (Figure 7B and Supporting Information Figure S4A). The body weights of tumors bearing TPRN-C, TPRN-CM, and TPN-CM rarely changed during the treatment. However, the body weights of mice treated with free MTO and TPRN-M were significantly reduced, and the mice died on the ninth day after administration (Figure S4A). The loaded MTO in TPRN-M leaked into the circulatory system before reaching the tumor site, leading to increased damage to healthy organs and resulting in serious toxic side effects. Meanwhile, the mice treated with PRN-CM that excluded the cyclic CRGDfK peptides lost weight on the tenth day after administration owing to the poor tumor targeting of the PRN-CM. As shown in Figure 7B, similar to the saline control group, the tumor volume in the TPRN-C-treated groups gradually increased with time, with no differences among them. However, when mice were treated with TPRN-CM,TPN-CM, or PRN-CM, tumor growth was greatly inhibited. Compared to the saline group, the tumor volume was obviously reduced to 30.0±9.6% for TPRN-CM, 66.6±11.3% for the TPN-CM and 51.9±8.5% for the PRN-CM, respectively. Meanwhile, the tumor growth index (TGI) calculated as the tumor volume at end time points compared to the initial time of drug treatment were used to evaluate the inhibitory effects on tumor growth.[44] The TGI was only 2.9±0.13 in the TPRN-CM group, suggesting the remarkable inhibition of TPRN-CM mediated chemo-chemodynamic therapy on tumor growth (Figure 7C). In addition, significant inhibition of tumor growth by TPRN-CM was confirmed by measuring the tumor weight of each group. At the end of the treatment period, tumor tissues were collected and weighed to evaluate their inhibitory effects on tumor growth (Figure 7D). Compared with the saline group, TPRN-CM treatment reduced tumor growth by 66.2%, which was significantly higher than that of TPN-CM (35.1%) and PRN-CM (50.4%). In contrast, TPRN-C also had a weak inhibitory effect on tumor growth (9.0%), which may be attributed to the involvement of Cu^{2+} in the nanosystem. Moreover, the therapeutic effect of TPRN-CM in tumors was evaluated using H&E staining and TUNEL assays, which are denoted as green fluorescence signals. As shown in Figure 7F, the highest level of apoptosis was observed in TPRN-CM-treated tumor tissue. Therefore, TPRN-CM exhibited a significant inhibitory effect on tumor growth, which was more effective than that of the other groups. In addition, the inhibitory effect of TPRN-CM on lung metastasis was evaluated. The lungs are major organs involved in the spread of cancer cells. At the end of the treatment period, the visually detected metastatic nodules in the lungs of each group were carefully recorded. As shown in Figure 7E, TPRN-CM treatment resulted in a 93.6% suppression of lung metastasis, which was significantly higher than that of TPN-CM and PRN-CM. Histological studies of lung tissues were conducted using H&E staining (Figure 7G). The metastatic lesions appeared as clusters of cells with deep nuclear staining.[39] The TPRN-CM treatment group showed almost no metastatic lesions, but significant metastatic lesions were observed in the other groups.

To further assess the toxicity of the nanoparticles to the major organs, the heart, liver, spleen, and kidney in each treatment group were evaluated by H&E staining (Figure 8). Compared with the saline injection control group, no obvious histological alterations were observed in the TPRN-C, TPN-CM, and TPRN-CM treatment groups, illustrating the good biocompatibility of these treatments. However, pyknosis in the liver and obvious alterations in the spleen were observed after PRN-CM treatment, indicating the toxic side effects of PRN-CM.

The in vivo therapeutic evaluations showed that the MTO and Cu^{2+} loaded nanosystem had good safety, with significant inhibition of primary tumor growth and notable prevention of lung metastasis compared with the MTO single-loaded nanosystem. Compared with TPN-CM and PRN-CM, TPRN-CM treatment showed a significant improvement in therapeutic effects, which could be largely due to the programmed targeting and penetration of primary tumors. The cyclic CRGDfK peptide in TPRN-CM specifically recognizes highly expressed $\alpha v\beta_{3/5}$ integrins in tumor vessels or cancer cells to endow the system with tumor-targeting ability, thereby ensuring accumulation in the tumor tissue. Moreover, the exposed r9 peptide of TPRN-CM in the tumor regions could significantly improve its specific accumulation in the primary tumor, promote its deep

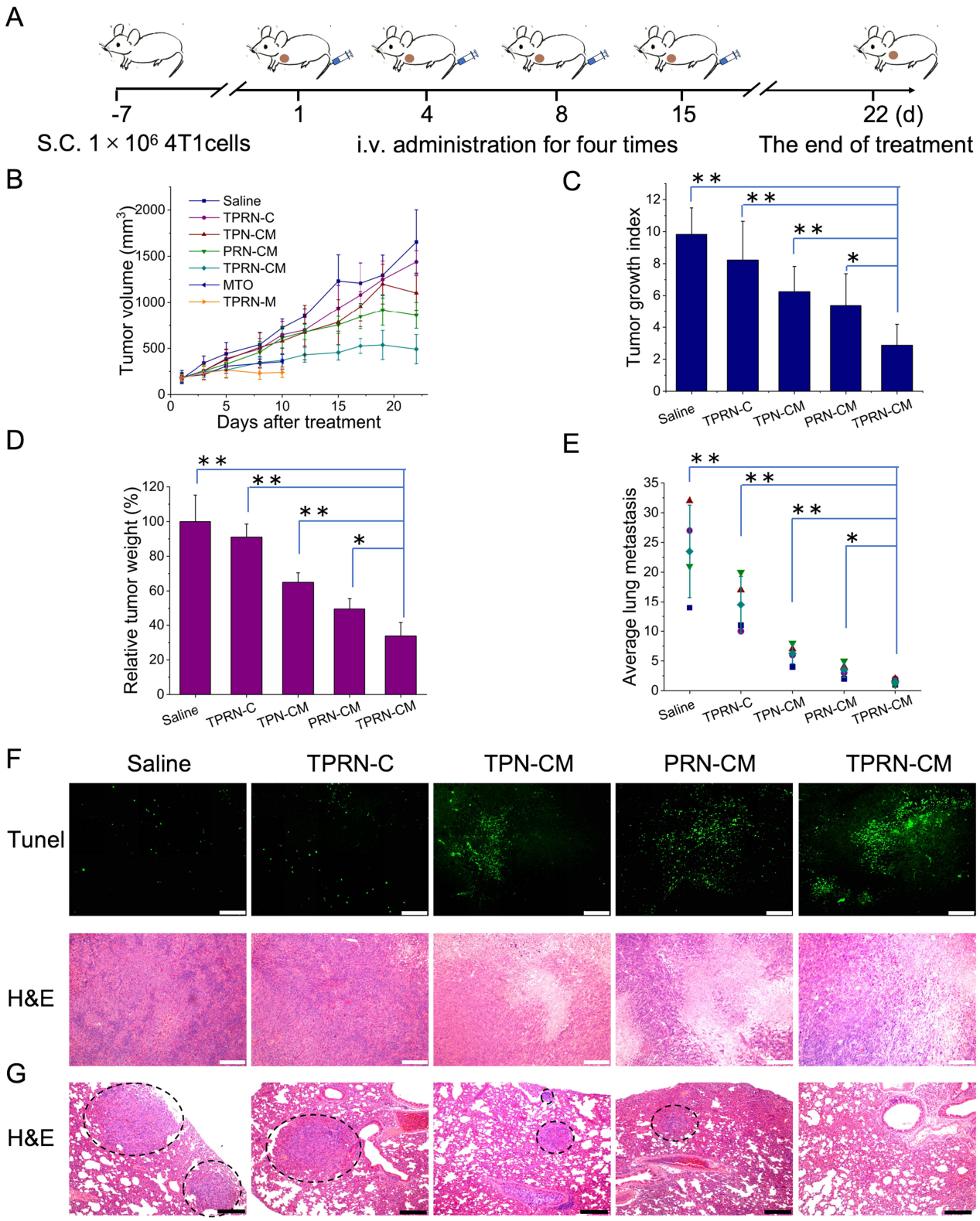

Figure 7 The in vivo therapeutic efficacy of TPRN-CM on tumor relapse and metastasis in the breast cancer model. (**A**) Administration scheme used in this study. (**B**) The tumor growth profiles, (**C**) tumor growth index, (**D**) the relative tumor weight, (**E**) the average number of lung metastatic nodules from each group in 4T1-induced tumor model. (**F**) The TUNEL and H&E assay of tumor from various formulations treated groups. The apoptosis was denoted as green fluorescence signals in the TUNEL assay, scale bar = 200 μm. (**G**) H&E examination of lung tissues from each group in the 4T1-induced metastatic model. Black arrows, metastatic lesion in lungs, scale bar=200 μm. The data are means±SD, **P* < 0.05, ***P*< 0.01.

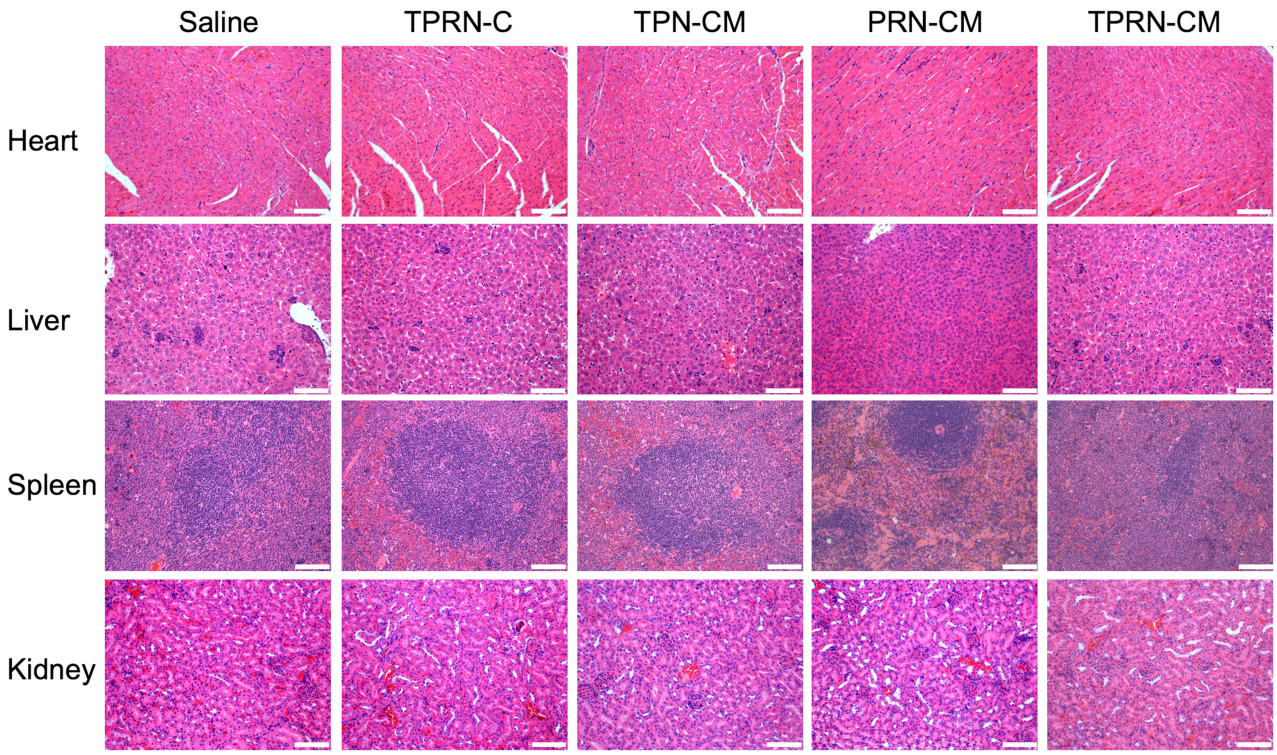

Figure 8 H&E staining of heart, liver, spleen and kidney from different treatment groups, scale bar=100 μm.

penetration into the tumor mass, and enhance its internalization into cancer cells. Furthermore, internalized MTO and Cu^{2+} can exert chemo-chemodynamic pharmacological effects. Therefore, the rationally designed TPRN-CM system with programmed targeting capability demonstrated great potential for breast cancer therapy.

Conclusion

In summary, we rationally designed a cyclic CRGDfK and r9 peptide-modified nanosystem of TPRN-CM with tumor targeting and deep tumor penetration in vivo for breast cancer therapy. The TPRN-CM system can load chemotherapeutic agents such as MTO and chemodynamic therapeutic agents such as Cu^{2+} for combined chemo-chemodynamic therapy of breast cancer. In a 4T1-induced tumor model, TPRN-CM displayed specific tumor accumulation, flexible permeation, and diffusion in the tumor mass, thereby producing a notable inhibition of tumor growth and lung metastasis. Therefore, rationally designed TPRN-CM provides a promising nanoplatform with efficient tumor targeting and penetration capability for effective anti-tumor therapy.

Ethics Approval

All animal experiments were performed in accordance with the GB/T 35892-2018 experimental animal welfare ethics review guide approved by the People's Republic of China and were reviewed and approved by the Institutional Animal Care and Use Committee (IACUC) of the Guangdong Medical Laboratory Animal Center (protocol no. B202311-19).

Acknowledgments

This work was supported by the Key Field Projects of the Guangdong Provincial Department of Education (No. 2022ZDZX2064), the Zhuhai Basic and Applied Basic Research Project (No. 2220004003125), and Guangdong Province Key Construction Discipline Research Capacity Enhancement Project (No. 2022ZDJS138). The animal

experiments of this work was accomplished with the help of Yi Wang from Guangdong Medical Laboratory Animal Center, Foshan 528000, People's Republic of China.

Disclosure

The authors declare no conflicts of interest in this work.

References

1. Heng S, Lu Z, Feng Y, et al. A novel navigated doxorubicin delivery formulation to breast cancer therapy. *Mater Today Adv*. 2022;14:100235. doi:10.1016/j.mtadv.2022.100235
2. J GW, Tjulandin S, Davidson N, et al. Phase III trial of nanoparticle albumin-bound paclitaxel compared with polyethylated castor oil–based paclitaxel in women with breast cancer. *J Clin Oncol*. 2005;23(31):7794–7803. doi:10.1200/JCO.2005.04.937
3. Zhou Y, Fan S, Feng L, et al. Manipulating intratumoral Fenton chemistry for enhanced chemodynamic and chemodynamic-synergized multimodal therapy. *Adv Mater*. 2021;33(48):2104223. doi:10.1002/adma.202104223
4. Fang Y, Huang S, Hu Q, et al. Injectable Zwitterionic Physical Hydrogel with Enhanced Chemodynamic Therapy and Tumor Microenvironment Remodeling Properties for Synergistic Anticancer Therapy. *ACS nano*. 2023;17(24):24883–24900. doi:10.1021/acsnano.3c05898
5. Wang X, Wang C, Tian H, et al. IR-820@ NBs Combined with MG-132 Enhances the Anti-Hepatocellular Carcinoma Effect of Sonodynamic Therapy. *Int j Nanomed*. 2023;31:6199–6212. doi:10.2147/IJN.S431910
6. Ren X, Wang N, Zhou Y, et al. An injectable hydrogel using an immunomodulating gelator for amplified tumor immunotherapy by blocking the arginase pathway. *Acta Biomater*. 2021;124:179–190. doi:10.1016/j.actbio.2021.01.041
7. Zhao P, Li H, Bu W. A forward vision for chemodynamic therapy: issues and opportunities. *Angew Chem Int Ed*. 2023;62(7):202210415. doi:10.1002/anie.202210415
8. Jana D, Zhao Y. Strategies for enhancing cancer chemodynamic therapy performance. *Exploration*. 2022;2(2):20210238. doi:10.1002/EXP.20210238
9. Li J, Dai J, Zhao L, et al. Bioactive bacteria/MOF hybrids can achieve targeted synergistic chemotherapy and chemodynamic therapy against breast tumors.*Adv Funct. Mater*. 2023;33(42):2303254.
10. Chen Z, Liu Z, Zhou Y, et al. Bionic aggregation-induced emission photosensitizer for enhanced cancer immunotherapy. *Mater Today Bio*. 2024;28:101217. doi:10.1016/j.mtbio.2024.101217
11. Ning S, Zhang T, Lyu M, et al. A type I AIE photosensitiser-loaded biomimetic nanosystem allowing precise depletion of cancer stem cells and prevention of cancer recurrence after radiotherapy. *Biomaterials*. 2023;295:122034. doi:10.1016/j.biomaterials.2023.122034
12. Ning S, Lyu M, Zhu D, et al. Type-I AIE photosensitizer loaded biomimetic system boosting cuproptosis to inhibit breast cancer metastasis and rechallenge. *ACS nano*. 2023;17(11):10206–10217. doi:10.1021/acsnano.3c00326
13. Liu Y, Zhu D, Zhu X, et al. Enhancing the photodynamic therapy efficacy of black phosphorus nanosheets by covalently grafting fullerene C_{60}. *Chem Sci*. 2020;11(42):11435–11442. doi:10.1039/D0SC03349A
14. Chen T, Luo X, Zhu L, et al. Biomimetic single-atom nanozyme system for efficient inhibition of gastric cancer ascites via SO_2 gas-enhanced nanocatalytic cancer therapy. *Chem Eng J*. 2023;467:143386. doi:10.1016/j.cej.2023.143386
15. Chen H, Luo X, Huang Q, et al. Platelet membrane fusion liposome loaded with type I AIE photosensitizer to induce chemoresistance cancer pyroptosis and immunogenic cell death for enhancing cancer immunotherapy. *Chem Eng J*. 2023;476:146276. doi:10.1016/j.cej.2023.146276
16. Sun R, Xiang J, Zhou Q, et al. The tumor EPR effect for cancer drug delivery: current status, limitations, and alternatives. *Adv. Drug Delivery Rev*. 2022;191:114614. doi:10.1016/j.addr.2022.114614
17. Li Y, Chen W, Kang Y, et al. Nanosensitizer-mediated augmentation of sonodynamic therapy efficacy and anti-tumor immunity. *Nat Commun*. 2023;14(1):6973. doi:10.1038/s41467-023-42509-7
18. Wang X, Zhang H, Chen X, et al. Overcoming tumor microenvironment obstacles: current approaches for boosting nanodrug delivery. *Acta Biomater*. 2023;166:42–68. doi:10.1016/j.actbio.2023.05.043
19. Li Z, Gao Y, Li W, et al. Charge-reversal nanomedicines as a smart bullet for deep tumor penetration. *Smart Mater Med*. 2022;3:243–253. doi:10.1016/j.smaim.2022.01.008
20. Stylianopoulos T, Jain RK. Combining two strategies to improve perfusion and drug delivery in solid tumors. *PNAS*. 2013;110(46):18632–18637. doi:10.1073/pnas.1318415110
21. Qiu ZW, Zhong YT, Lu ZM, et al. Breaking physical barrier of fibrotic breast cancer for photodynamic immunotherapy by remodeling tumor extracellular matrix and reprogramming cancer-associated fibroblasts. *ACS nano*. 2024;18(13):9713–9735. doi:10.1021/acsnano.4c01499
22. Li M, Wang Y, Zhang L, et al. Cancer Cell Membrane-Enveloped Dexamethasone Normalizes the Tumor Microenvironment and Enhances Gynecologic Cancer Chemotherapy. *ACS nano*. 2023;17(17):16703–16714. doi:10.1021/acsnano.3c03013
23. Xing Y, Xiu J, Zhou M, et al. Copper single-atom jellyfish-like nanomotors for enhanced tumor penetration and nanocatalytic therapy. *ACS nano*. 2023;17(7):6789–6799. doi:10.1021/acsnano.3c00076
24. Zhou M, Zou X, Cheng K, et al. The role of cell-penetrating peptides in potential anti-cancer therapy. *ClinTransl Med*. 2022;12(5):822.
25. Rusiecka I, Gągało I, Kocić I. Cell-penetrating peptides improve pharmacokinetics and pharmacodynamics of anticancer drugs. *Tissue Barriers*. 2022;10(1):1965418. doi:10.1080/21688370.2021.1965418
26. Kanasty R, Dorkin JR, Vegas A, et al. Delivery materials for siRNA therapeutics. *Nat Mater*. 2013;12(11):967–977. doi:10.1038/nmat3765
27. He B, Tan T, Wang H, et al. Rational design of tumor microenvironment-activated micelles for programed targeting of breast cancer metastasis. *Adv Funct Mater*. 2018;28(8):1705622. doi:10.1002/adfm.201705622
28. Zorko M, Jones S, Ü L. Cell-penetrating peptides in protein mimicry and cancer therapeutics. *Adv Drug Deliv Rev*. 2022;180:114044. doi:10.1016/j.addr.2021.114044
29. Ma S, Li Y, Liu F, et al. Hierarchical-unlocking virus-esque NanoCRISPR precisely disrupts autocrine and paracrine pathway of VEGF for tumor inhibition and antiangiogenesis. *J Control Release*. 2024;366:505–518. doi:10.1016/j.jconrel.2024.01.001

30. Wu GL, Liu F, Li N, et al. Trisulfide Bond-Mediated Molecular Phototheranostic Platform for "Activatable" NIR-II Imaging-Guided Enhanced Gas/Chemo-Hypothermal Photothermal Therapy. *Adv Sci*. 2023;10(36):2304104. doi:10.1002/advs.202304104
31. Sanati M, R AA, Aminyavari S, et al. RGD-engineered nanoparticles as an innovative drug delivery system in cancer therapy. *J Drug Deliv Sci Tec*. 2023:104562. DOI:10.1016/j.jddst.2023.104562
32. Cao H, Zou L, He B, et al. Albumin biomimetic nanocorona improves tumor targeting and penetration for synergistic therapy of metastatic breast cancer. *Adv Funct Mater*. 2017;27(11):1605679. doi:10.1002/adfm.201605679
33. Tan T, Wang Y, Wang J, et al. Targeting peptide-decorated biomimetic lipoproteins improve deep penetration and cancer cells accessibility in solid tumor. *Acta Pharmaceutica Sinica B*. 2020;10(3):529–545. doi:10.1016/j.apsb.2019.05.006
34. Feng Q, Bennett Z, Grichuk A, et al. Severely polarized extracellular acidity around tumour cells. *Nat Biomed Eng*. 2024;4:1–3.
35. Yang X, Xu C, Zhang X, et al. Development of sulfonamide-functionalized charge-reversal AIE photosensitizers for precise photodynamic therapy in the acidic tumor microenvironment. *Adv Funct Mater*. 2023;33(30):2300746. doi:10.1002/adfm.202300746
36. Du H, Zhao S, Wang Y, et al. pH/Cathepsin B hierarchical-responsive nanoconjugates for enhanced tumor penetration and chemo-immunotherapy. *Adv Funct Mater*. 2020;30(39):2003757. doi:10.1002/adfm.202003757
37. Zeng X, Li P, Yan S, et al. Reduction/pH-responsive disassemblable MOF-microbial nanohybrid for targeted tumor penetration and synergistic therapy. *Chem Eng J*. 2023;452:139517. doi:10.1016/j.cej.2022.139517
38. Duan H, Liu C, Hou Y, et al. Sequential delivery of quercetin and paclitaxel for the fibrotic tumor microenvironment remodeling and chemotherapy potentiation via a dual-targeting hybrid micelle-in-liposome system. *ACS Appl Mater Inter*. 2022;14(8):10102–10116. doi:10.1021/acsami.1c23166
39. Wu M, Qu R, Li H, et al. Semiconducting polymer nanomanipulators for thermal sensitization and metastasis-inhibited synergistic cancer therapy. *Nano Today*. 2023;48:101691.
40. Luo T, Jiang X, Li J, et al. Phosphate Coordination to Metal-Organic Layer Secondary Building Units Prolongs Drug Retention for Synergistic Chemoradiotherapy. *Angew Chem*. 2024;202319981.
41. Chen Z, Li S, Li F, et al. DNA Damage Inducer Mitoxantrone Amplifies Synergistic Mild-Photothermal Chemotherapy for TNBC via Decreasing Heat Shock Protein 70. Expression. *Adv Sci*. 2023;10(16):2206707. doi:10.1002/advs.202206707
42. Zuo W, Fan Z, Chen L, et al. Copper-based theranostic nanocatalysts for synergetic photothermal-chemodynamic therapy. *Acta Biomater*. 2022;147:258–269. doi:10.1016/j.actbio.2022.05.030
43. N HY, X ZW, R GY, et al. State-of-The-art advances of copper-based nanostructures in the enhancement of chemodynamic therapy. *J Mater Chem B*. 2021;9(2):250–266. doi:10.1039/D0TB02360D
44. Sun R, Zhang Y, Lin X, et al. Aminopeptidase N-Responsive Conjugates with Tunable Charge-Reversal Properties for Highly Efficient Tumor Accumulation and Penetration. *Angew Chem Int Ed*. 2023;62(9):202217408. doi:10.1002/anie.202217408
45. Zhang P, Chen D, Li L, et al. Charge reversal nano-systems for tumor therapy. *J Nanobiotechnol*. 2022;20:1–27.
46. Bao Y, Zhang H, Wu X, et al. Dual-Responsive Cu (I) and Cu (II) Co-Doped Carbon Dots for Synergistic Chemodynamic-Photothermal anti-tumor Therapy. *ACS Appl Nano Mater*. 2023;6(15):14410–14420. doi:10.1021/acsanm.3c02418
47. Summonte S, F RG, Lopedota A, et al. Thiolated polymeric hydrogels for biomedical application: cross-linking mechanisms. *J Control Release*. 2021;330:470–482. doi:10.1016/j.jconrel.2020.12.037
48. Meng X, Zhang X, Lei Y, et al. Biodegradable copper–metformin nanoscale coordination polymers for enhanced chemo/chemodynamic synergistic therapy by reducing oxygen consumption to promote H 2 O 2 accumulation. *J Mater Chem B*. 2021;9(8):1988–2000. doi:10.1039/D0TB02476G
49. Wu X, Yang M, S KJ, et al. Reactivity differences enable ROS for selective ablation of bacteria. *Angew Chem*. 2022;134(17):202200808. doi:10.1002/ange.202200808
50. Akkoc Y, Dalci K, E KH, et al. Tumor-derived CTF1 (cardiotrophin 1) is a critical mediator of stroma-assisted and autophagy-dependent breast cancer cell migration, invasion and metastasis. *Autophagy*. 2023;19(1):306–323. doi:10.1080/15548627.2022.2090693
51. Gong XT, Zhuang J, Chong KC, et al. Far-Red Aggregation-Induced Emission Hydrogel-Reinforced Tissue Clearing for 3D Vasculature Imaging of Whole Lung and Whole Tumor. *Adv Mater*. 2024;36(35):2402853. doi:10.1002/adma.202402853